Supplementary Information

Metal-Organic Framework derived Inverse Opal type Porous Graphitic Carbon for Highly Stable Lithium-ion Batteries

Nitish Kumar, Prakash Kumar Pathak, and Rahul R. Salunkhe*

Department of Physics, Indian Institute of Technology Jammu Jagti, NH-44, PO Nagrota Jammu, 181 221, J&K, India

* Corresponding author

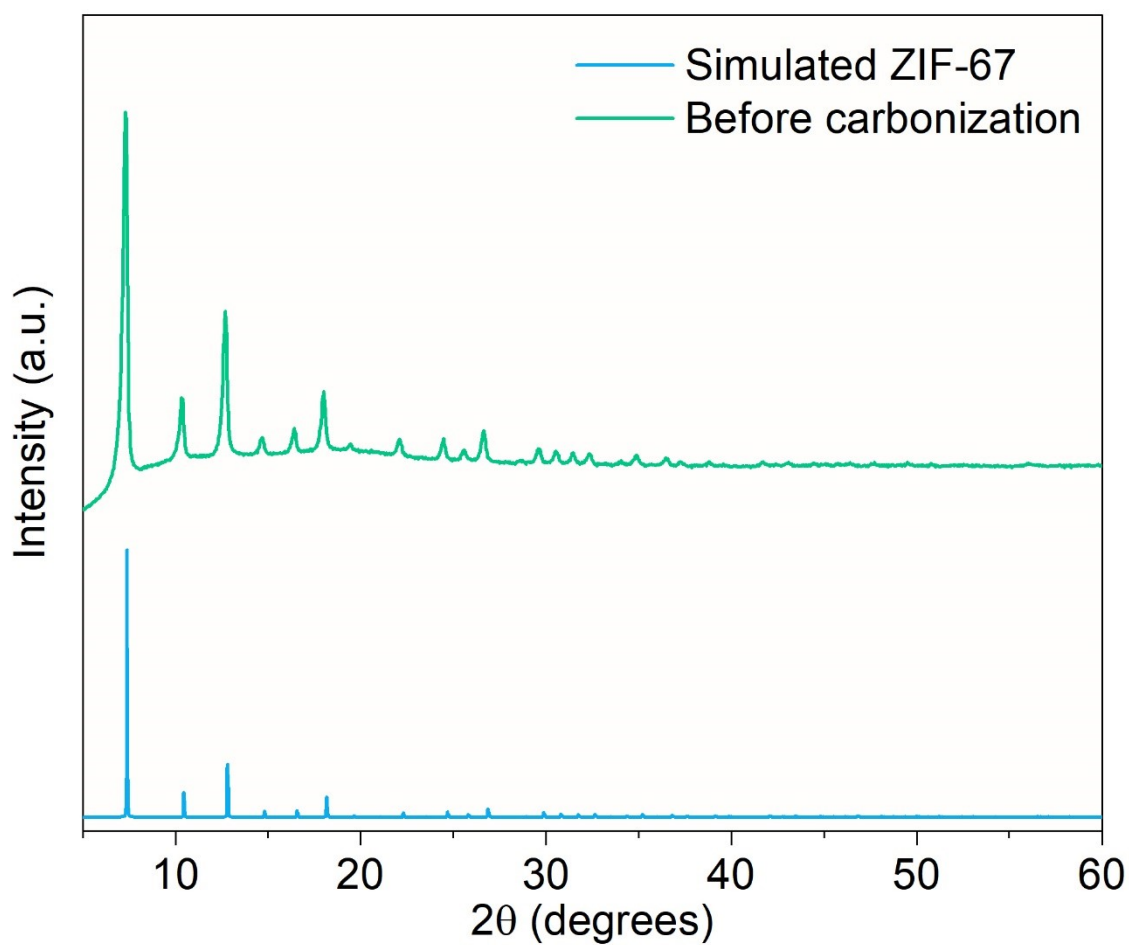rahul.salunkhe@iitjammu.ac.in (Rahul R. Salunkhe)

Fig. S1. Simulated XRD pattern of ZIF-67 and experimental XRD pattern obtained for PS-ZIF-67 precursor powder. Amorphous hump and peak broadness come from the composite material's PS particles. The sharp and correctly positioned crystalline peaks validate the synthesis of ZIF-67 particles.

Table S1. Atomic percentages of various elements in different samples as calculated by survey

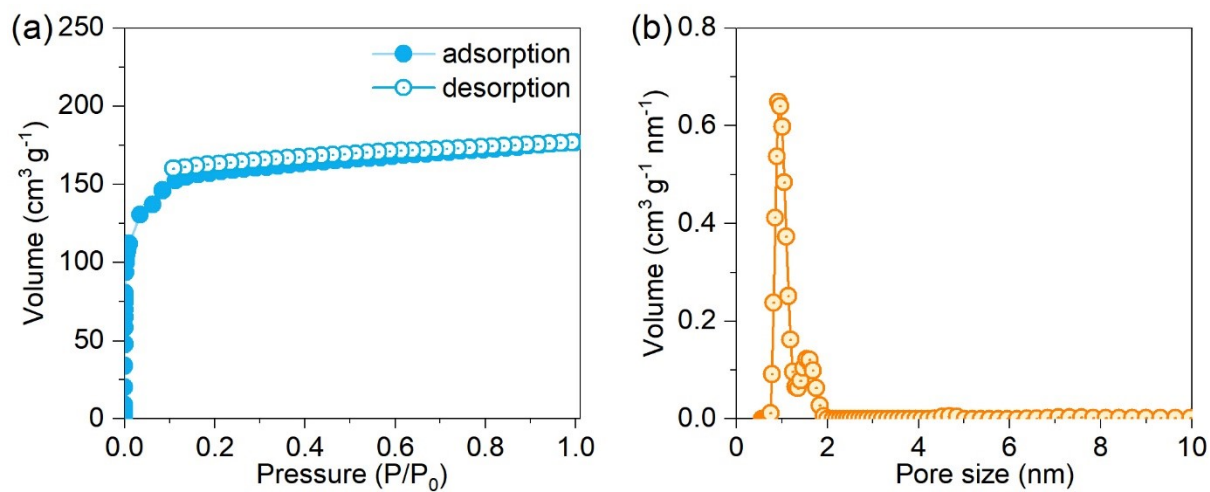| Sample Code	Elements (at.%)			
	C	N	O	Co
PS-ZIF-67	70.9	18.2	5.1	4.9
C-600	91.55	4.3	4.1	0.95
C-700	88.35	4.9	6.4	0.35
C-800	91.8	3.5	4.5	0.2
C-900	93.9	2.1	3.85	0.15

spectra.

Fig. S2. (a) Nitrogen adsorption-desorption isotherms for PS-ZIF-67 sample, and (b) pore size distribution showing the presence of micropores developed by the attachment of ZIF-67 particles over the PS surface.
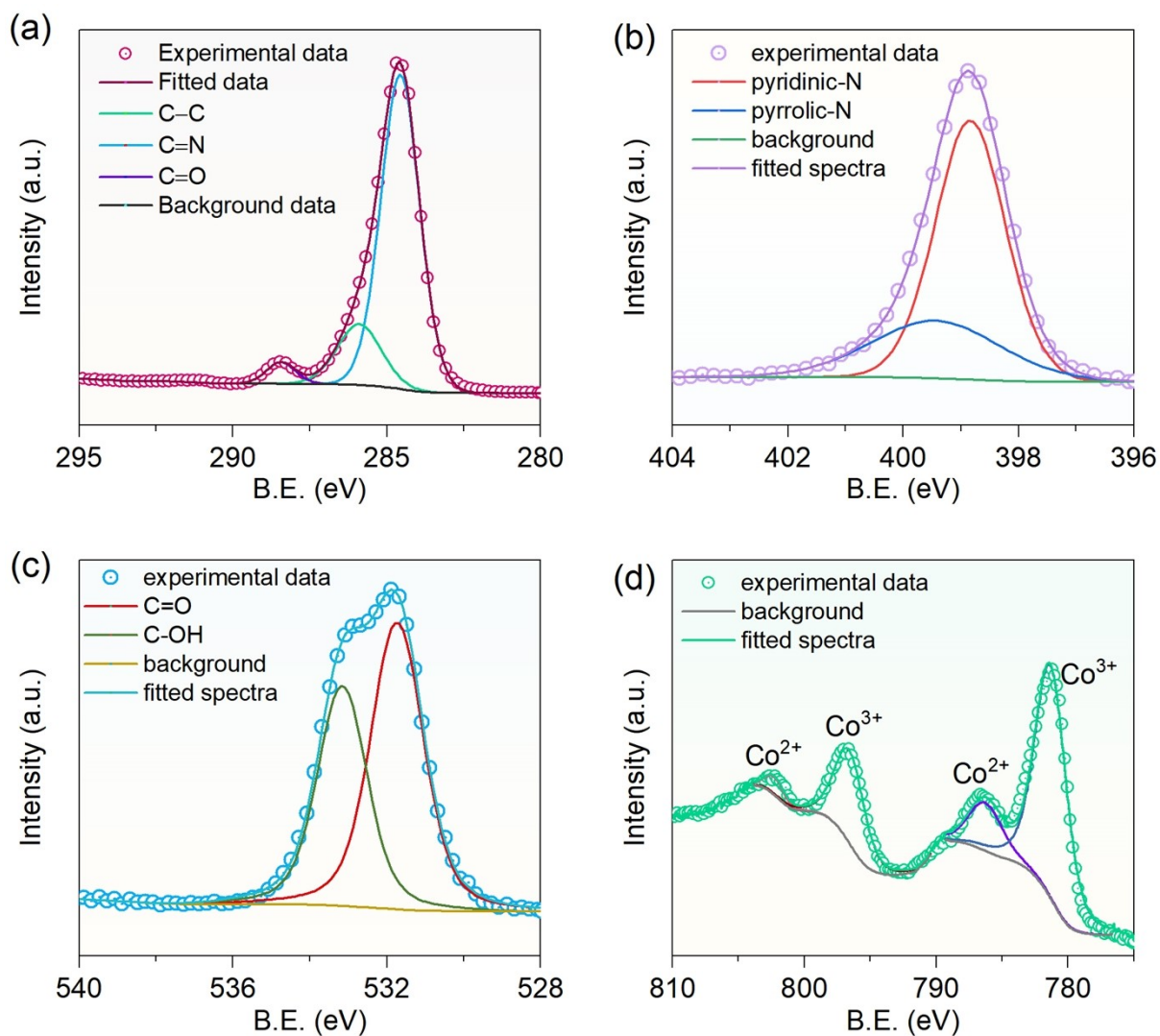
Fig. S3. The high-resolution narrow region deconvoluted spectra for (a) C 1s, (b) N 1s, (c) O 1s, and (d) Co elements.

Table S2. Raman peak positions for different observed bands.

Sample	D	G	2D
C-600	1342	1594	2682
C-700	1347	1589	2686
C-800	1343	1583	2683
C-900	1343	1580	2683

Table S3. Atomic percentages of various deconvoluted bonding in different samples.

| Element code	Different deconvoluted peaks position and atomic percentages (eV, at. %)			
C 1s	C=C	C-C/ C=N	C=O	C(O)-O
C-600	284.5, 51.8	285.2, 16.48	286.6, 25.12	289.3, 6.58
C-700	284.3, 54.3	284.9, 25.7	286, 12.3	288.5, 7.7
C-800	284.4, 55.8	284.9, 15.9	285.8, 21.6	288.6, 6.7
C-900	284.5, 76.4	-	286, 16	288.7, 7.6
N 1s	Pyridinic-N	Pyrrolic-N		NO$_2$
C-600	398.6, 39.20	400.6, 50.88		404.2, 10.1
C-700	398.4, 54.5	400, 45.5		-
C-800	-	399.7, 100		-
C-900	-	399.8, 100		-
O 1s	C-O	C=O		
C-600	532.4, 64.5	533.8, 46.5		
C-700	532.2, 75.1	533.7, 24.9		
C-800	531.9, 53	533.3, 47		
C-900	532.1, 58.1	533.4, 41.9		
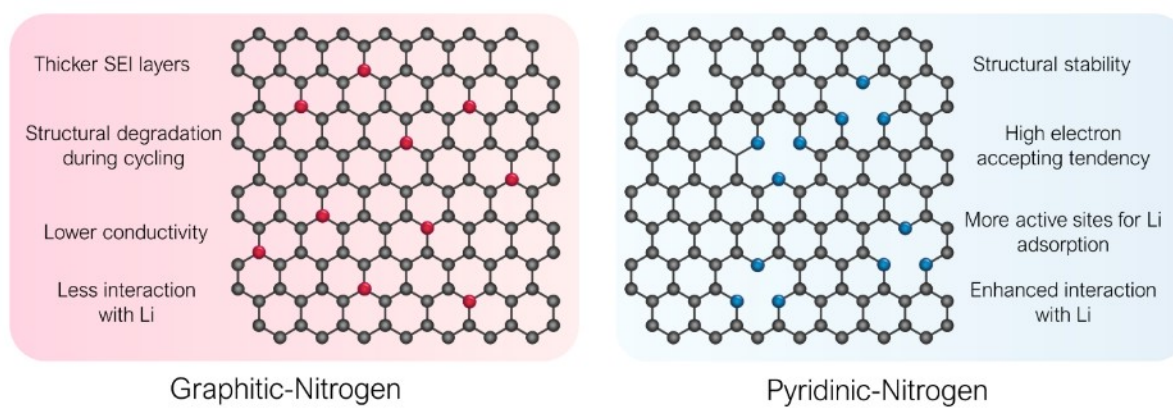
Fig. S4. Schematic representation of graphitic-N and pyridinic-N contents in graphene structure. The limitations of graphitic-N sites and the advantages of pyridinic-N sites are also highlighted.[1]
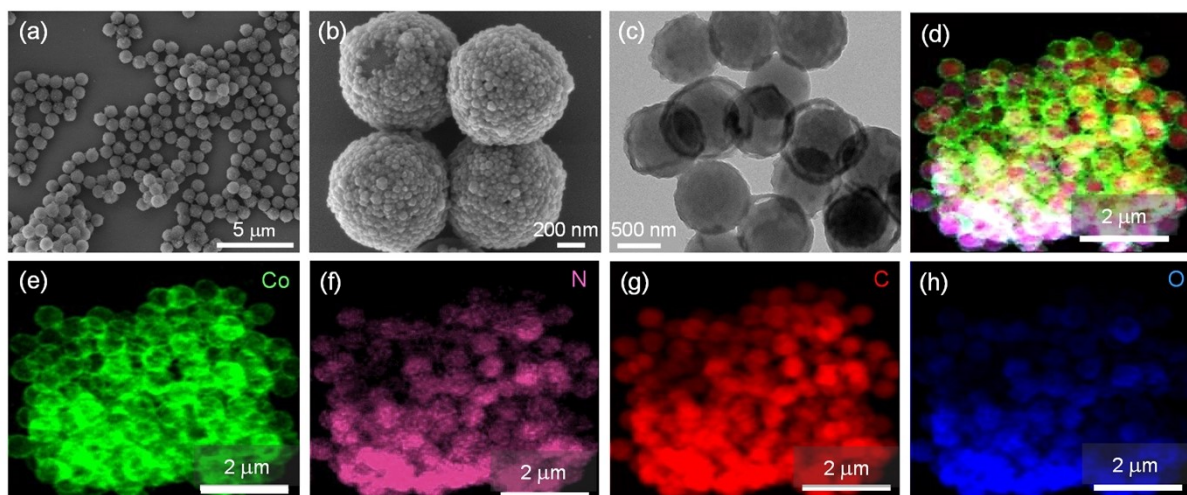
Fig. S5. FESEM images of PS-ZIF-67 sample. (a) The low magnification image shows the homogeneity of the developed sample, and (b) shows a PS core decorated with small-sized ZIF-67 particles. TEM studies for morphology and elemental distribution for PS-ZIF-67. (c) The bright field TEM image shows the PS core and ZIF-67 shell type of morphology. (d) The overlapped image for the region used for the EDS study and EDS mappings for (e) Co, (f) N, (g) C, and (h) O elements.
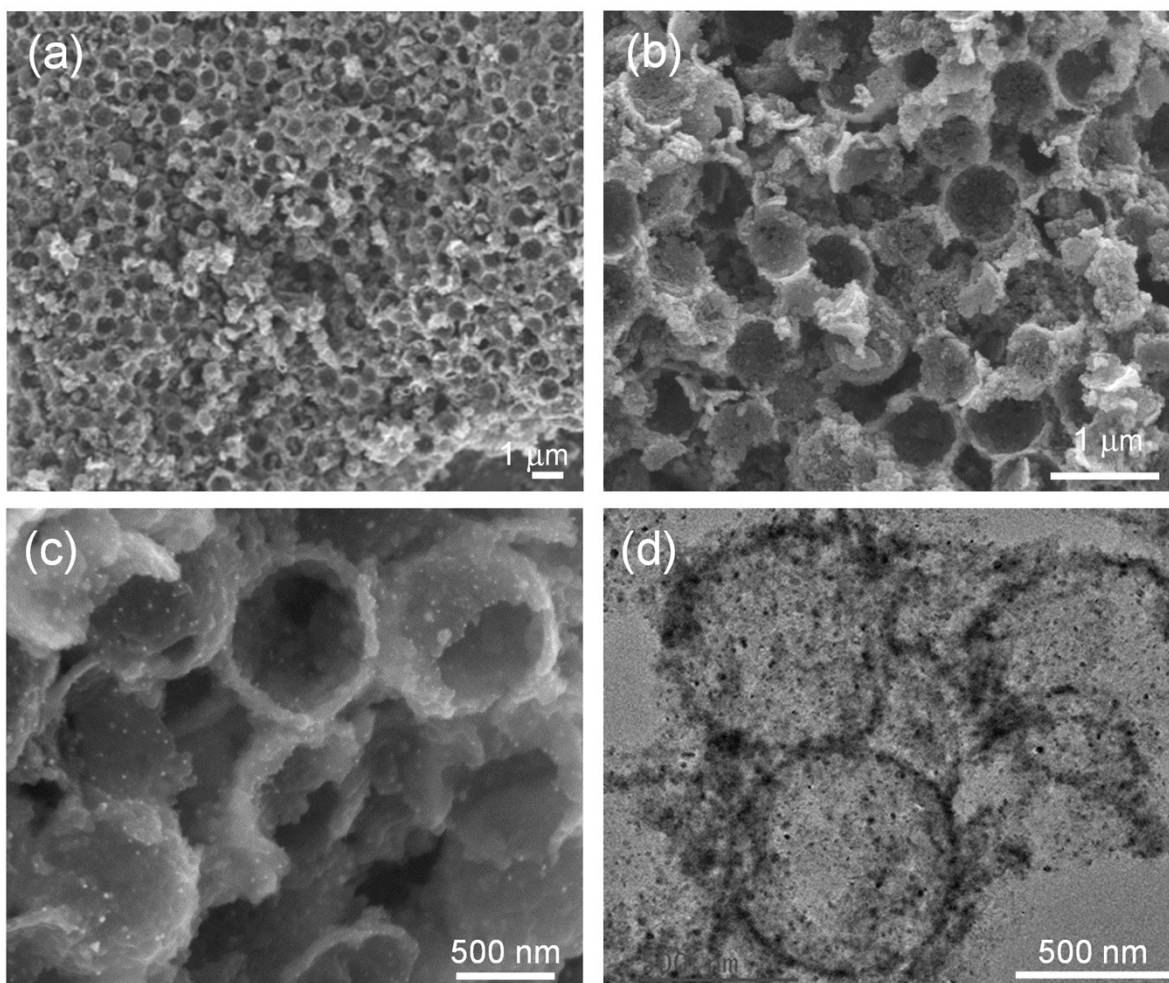
Fig. S6. Comprehensive morphological studies for C-700 sample. (a) Low magnification FESEM image shows the homogeneously developed 3D porous network in C-700, and (b) the image demonstrates the removal of the PS core. (c) High-magnification FESEM image depicts the hollow structure formed for the C-700 sample. (d) HRTEM image at low magnification showing the C-700 sample's morphology.
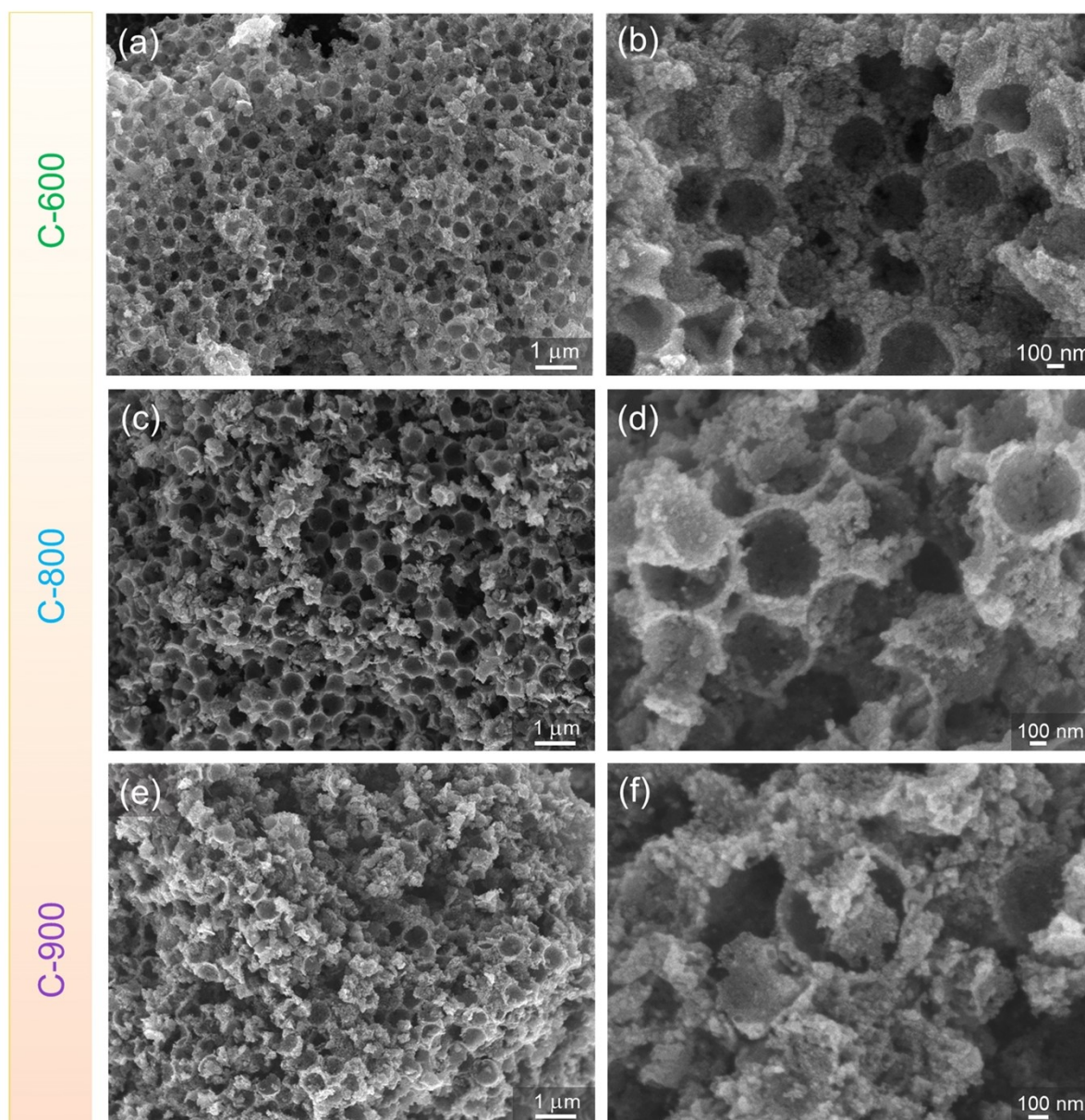
Fig. S7. FESEM images of C-600, C-800 and C-900 samples. (a) 3D porous structure, and (d) a high-resolution image of C-600. (c) The low magnification image and (d) the high magnification image shows a highly porous structure of C-800. (e) FESEM image shows a 3D porous structure at low magnification, and (f) the porous structure collapses due to the high-temperature treatment for C-900.

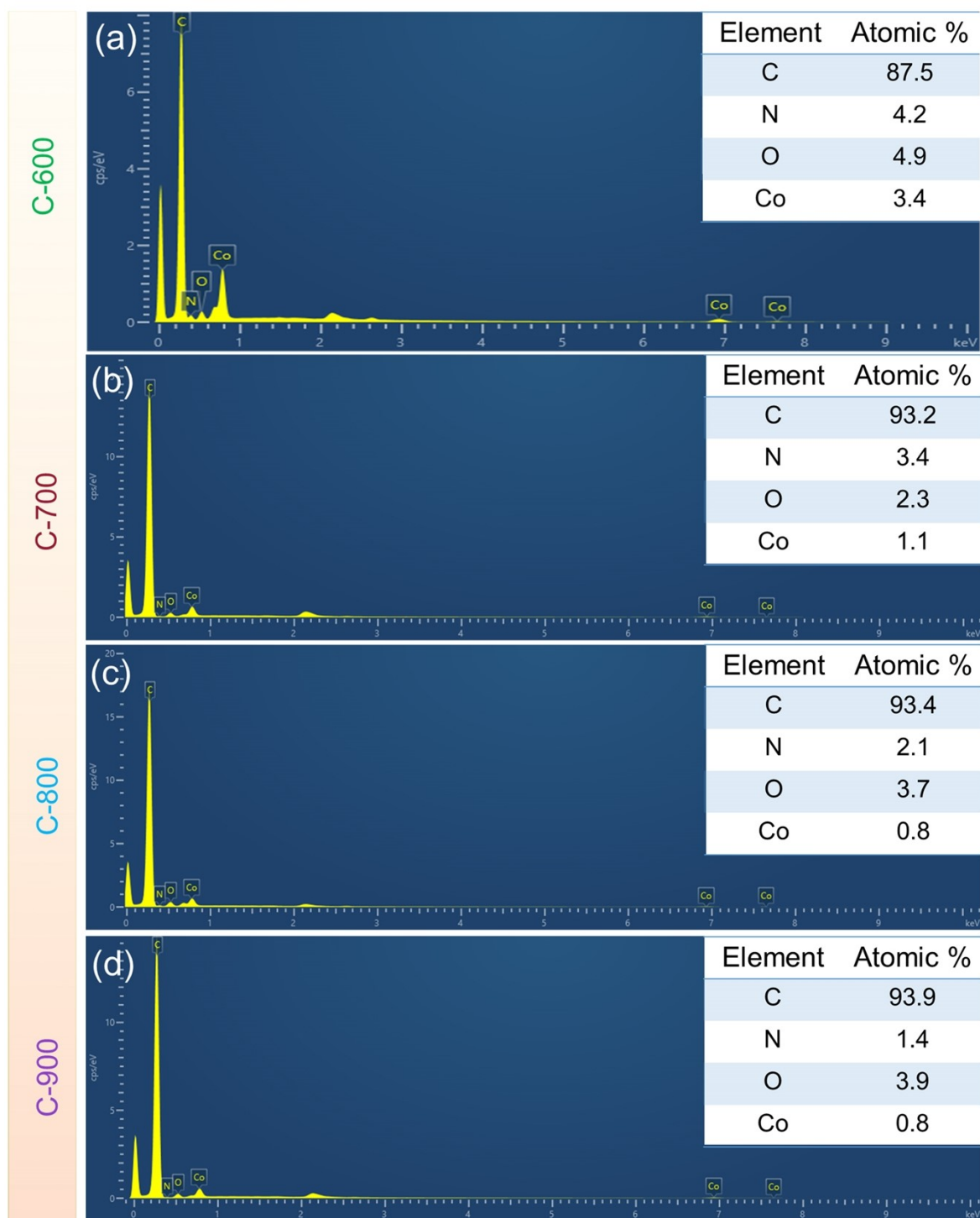**Fig. S8**. EDS spectra show the presence of different elements in various carbonized samples, namely (a) C-600, (b) C-700, (c) C-800, and (d) C-900. The inset tables show the corresponding elements' atomic percentages.
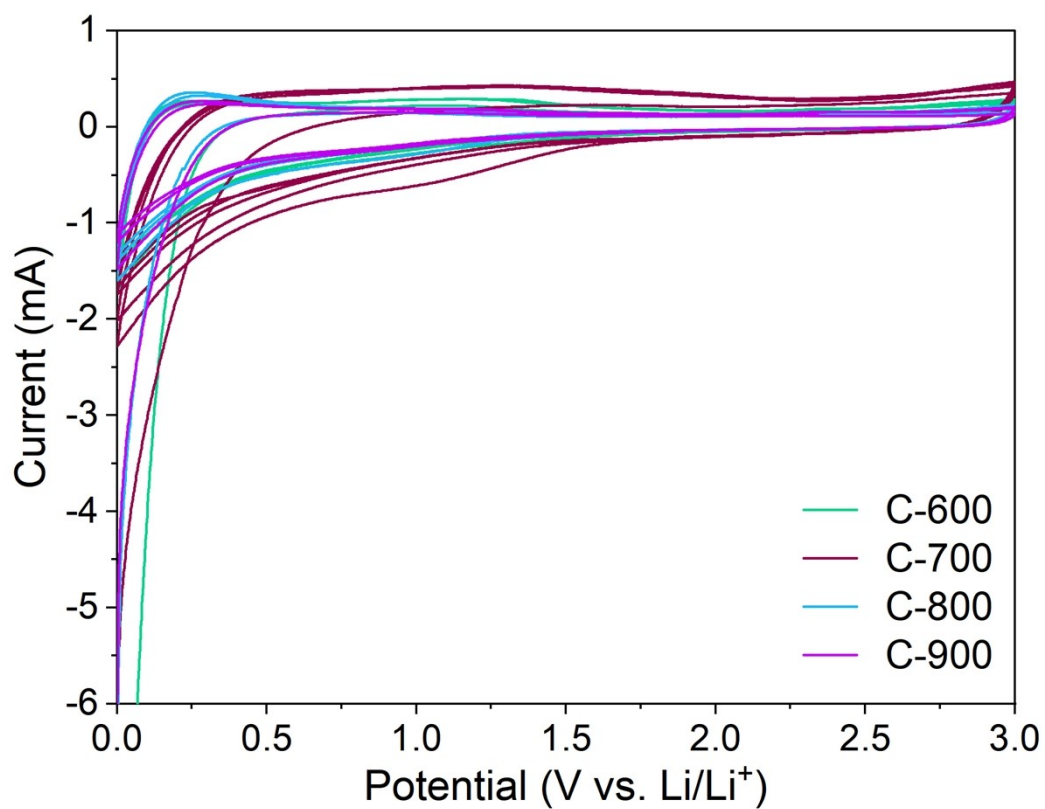
Fig. S9. Comparative precycling data for different samples at a scan rate of 1 mV s^{-1}.
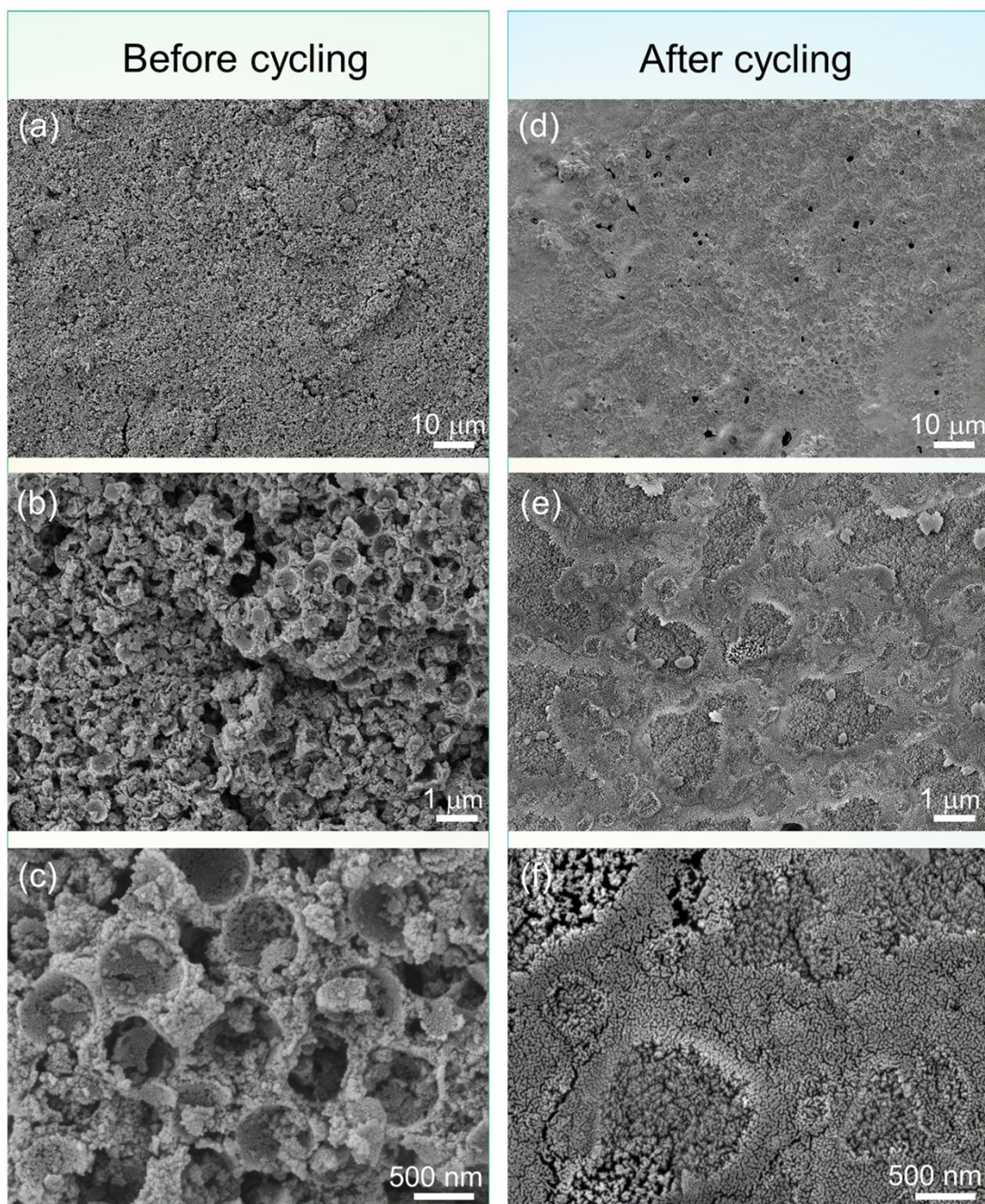
Fig. S10. FESEM images of (a-c) the fresh coin cell, and after long cycle testing (d-f) at different magnifications.

Element	Atomic %
C	41.2
N	0.6
O	44.8
F	3.4
P	1.1

Fig. S11. EDS studies after long cycle testing. (a) EDS spectra showing the elemental composition, (b) EDS layered image showing overlapped elements, and mapping of elements (c) C, (d) O, (e) N, (f) P, and (g) F. The scale bar is 1 μm in length.

Table S4 Performance comparison of our sample with previous literature reports.

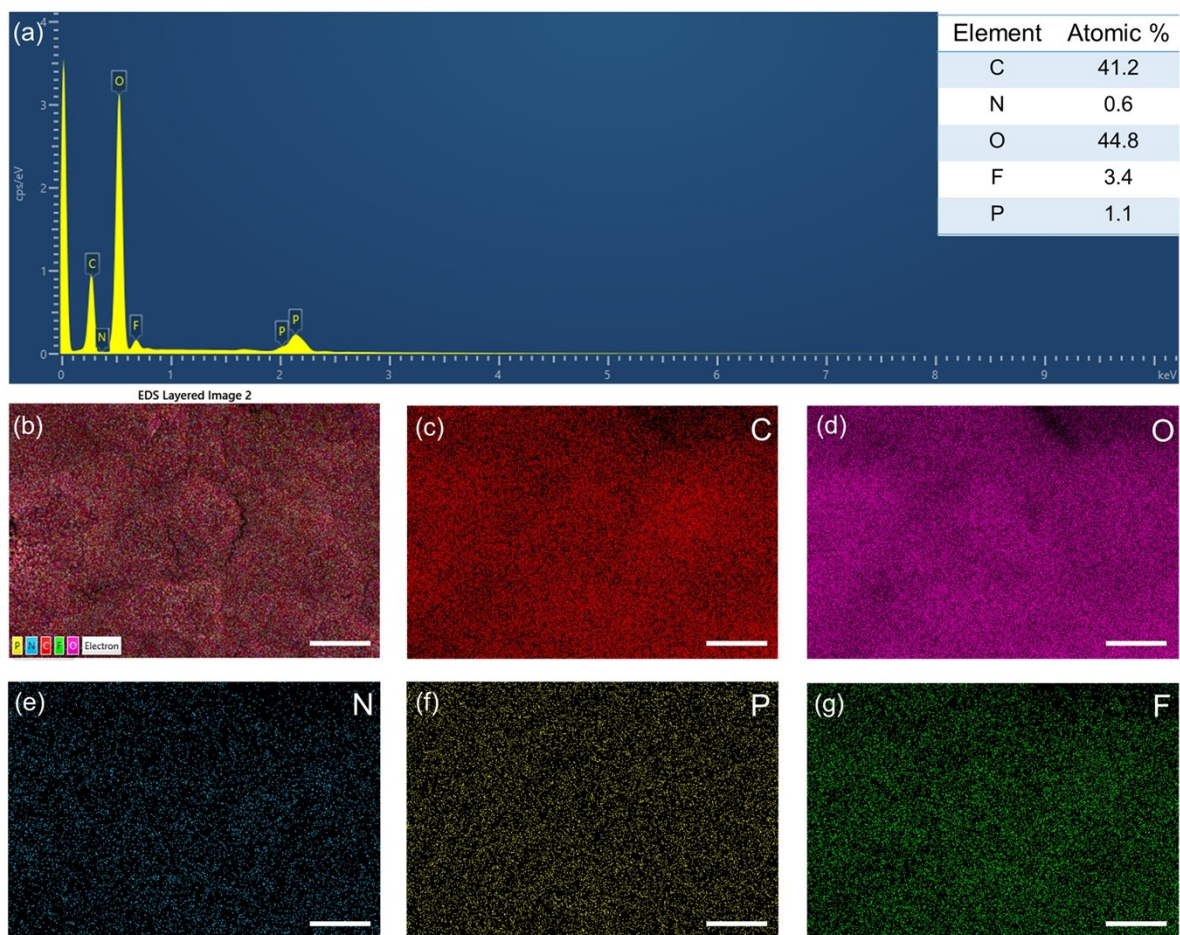| No.	Material	Specific capacity with current density (mA h g^{-1})	No. of cycles tested with current density	Cyclic retention (%)	Ref.
1.	Nitrogen-deficient g-C$_3$N$_4$	647 at 100 mA g^{-1}	5000 at 1 A g^{-1}	-	[2]
2.	TiO$_2$(B)/Carbon Core/Shell Nanotubes	479.2 at 1 C	1000 at 1C	~100	[3]
3.	Porous GC from coal tar pitch	707 at 0.05 A g^{-1}	1000 at 1 A g^{-1}	93.5	[4]
4.	Biomass-derived GC	471 at 100 mA g^{-1}	-	-	[5]
5.	Porous GC Nanosheets	722 at 100 mA g^{-1}	570 at 30 C	65	[6]
6.	H-TiO$_2$/GC hollow spheres	225 at 100 mA g^{-1}	1000 at 1 A g^{-1}	92	[7]
7.	Ni$_2$P/GC nanostructure	385 at 100 mA g^{-1}	200 at 100 mA g^{-1}	87.3	[8]
8.	CoSe/Co@N doped GC	630 at 200 mA g^{-1}	-	-	[9]
9.	Nitrogen-doped carbons with ultrafine Sn particles embedded	408 at 100 mA g^{-1}	-	-	[10]
10.	Highly GC derived from Coconut Coir Waste	397 at 0.05 C	-	-	[11]
11.	Chitosan-derived graphitic carbon@Fe$_3$C	423 at 100 mA g^{-1}	200 at 2 A g^{-1}	85	[12]
12.	ZnO/3D OMC	673 at 0.1 C	300	-	[13]
13.	ZnO/3D OM-mC	973.3 at 0.1 C	100	-	[14]
14.	TiO$_2$–CN	549 at 0.2 C	100	-	[15]
15.	3DOM ZnO/CC	911 at 0.1 A g^{-1}	100	-	[16]
16.	C@Fe$_2$O$_3$@SnO$_2$	388 at 0.1 A g^{-1}	200		[17]
17.	CoO@3D OMC	673.3 at 2 A g^{-1}	1000		[18]
18.	3DOM SnO$_2$	653 at 2 C	50	52	[19]
19.	Rutile TiO$_2$ Inverse Opal	608 at 75 mA g^{-1}	1000	53	[20]
20.	Natural graphite	360.9 at 0.1 C	200	89	[21]
21.	**C-700**	**755 at 50 mA g^{-1}** **805 after 65 cycles**	**2000 at 1 A g^{-1}**	**96%**	**This work**

* GC= graphitic carbon, 3D= three dimensional, OMC= ordered macroporous carbon, OM-mC = ordered macro-mesoporous carbon, CN= Carbon nanocomposites, 3DOM= three dimensional ordered macroporous,

Note S1.

The reaction kinetics can be explained by Dunn's method, which provides information about diffusion-controlled processes. The current calculated from this method is

$$i = av^b \tag{1}$$

$$I(v) = k_1 (v)^{0.5} + k_2 v \tag{2}$$

$$\frac{I(v)}{v^{0.5}} = k_1 + k_2 v^{0.5} \tag{3}$$

Where $I(v) \propto v \Rightarrow k_1 v$ = capacitive current

$I(v) \propto v^{0.5} \Rightarrow k_1 v^{0.5}$ = Diffusion-controlled current.

Where k_1, k_2, and are intercept, slope, and scan rates for C-700 at different scan rates ($0.2 - 2$ mV s^{-1}).

In addition, the Galvanostatic Intermittent Titration Technique (GITT) was used to quantify the ions' diffusion coefficients, which were then estimated using equation (7), shown below.

The formula for determining GITT using *Fick's second law*[22]:

$$D = \frac{4L^2}{\pi \tau} \left(\frac{\Delta E_s}{\Delta E_\tau} \right)^2 \tag{4}$$

Here, L is the ion diffusion distance (cm), and the pulse time of the current pulse is denoted by τ (s). "ΔE_s" is the voltage difference measured at the end of the relaxation period for two successive steps, and "ΔE_τ" is the difference between the initial voltage and final voltage during the discharge pulse time after eliminating the IR drop.
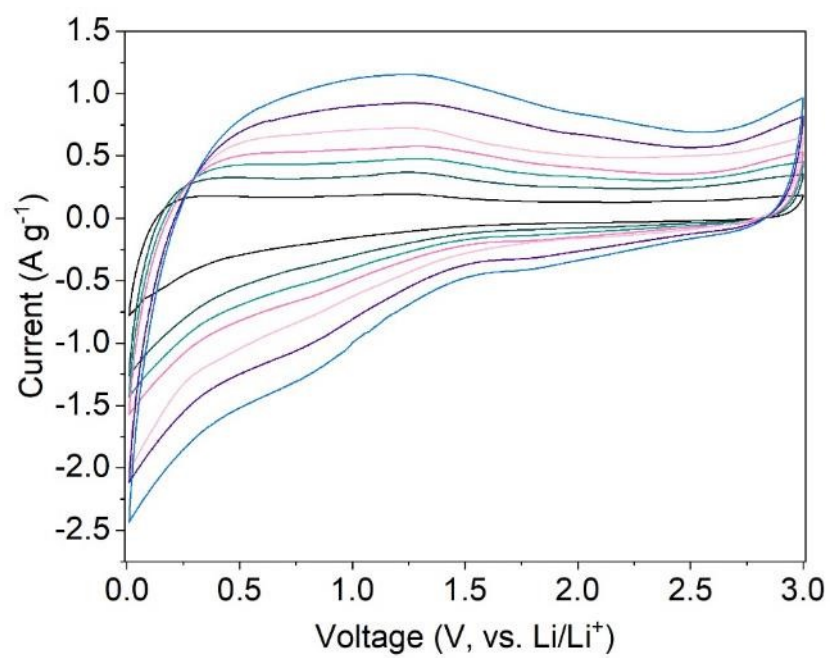
Fig. S12. CV curves at different scan rates varying from 0.2 to 2 mV s^{-1}. Dunn's method used these scan rates for "b" value calculations.

References

(1) Ma, C.; Shao, X.; Cao, D. Nitrogen-Doped Graphene Nanosheets as Anode Materials for Lithium Ion Batteries: A First-Principles Study. *J. Mater. Chem.* **2012**, *22* (18), 8911–8915.

(2) Sun, S.; Wu, Y.; Zhu, J.; Lu, C.; Sun, Y.; Wang, Z.; Chen, J. Stabilizing Plasma-Induced Highly Nitrogen-Deficient g-C3N4 by Heteroatom-Refilling for Excellent Lithium-Ion Battery Anodes. *Chem. Eng. J.* **2022**, *427*, 131032.

(3) Zhu, X.; Yang, X.; Lv, C.; Guo, S.; Li, J.; Zheng, Z.; Zhu, H.; Yang, D. New Approach to Create TiO 2 (B)/Carbon Core/Shell Nanotubes: Ideal Structure for Enhanced Lithium Ion Storage. *ACS Appl. Mater. Interfaces* **2016**, *8* (29), 18815–18821.

(4) Xing, B.; Zhang, C.; Liu, Q.; Zhang, C.; Huang, G.; Guo, H.; Cao, J.; Cao, Y.; Yu, J.; Chen, Z. Green Synthesis of Porous Graphitic Carbons from Coal Tar Pitch Templated by Nano-CaCO3 for High-Performance Lithium-Ion Batteries. *J. Alloys Compd.* **2019**, *795*, 91–102.

(5) Han, S.-W.; Jung, D.-W.; Jeong, J.-H.; Oh, E.-S. Effect of Pyrolysis Temperature on Carbon Obtained from Green Tea Biomass for Superior Lithium Ion Battery Anodes. *Chem. Eng. J.* **2014**, *254*, 597–604.

(6) Chen, L.; Wang, Z.; He, C.; Zhao, N.; Shi, C.; Liu, E.; Li, J. Porous Graphitic Carbon Nanosheets as a High-Rate Anode Material for Lithium-Ion Batteries. *ACS Appl. Mater. Interfaces* **2013**, *5* (19), 9537–9545.

(7) Liu, H.; Li, W.; Shen, D.; Zhao, D.; Wang, G. Graphitic Carbon Conformal Coating of Mesoporous TiO 2 Hollow Spheres for High-Performance Lithium Ion Battery Anodes. *J. Am. Chem. Soc.* **2015**, *137* (40), 13161–13166.

(8) Kim, Y.-S.; Kim, M.-C.; Moon, S.-H.; Kim, H.; Park, K.-W. Ni2P/Graphitic Carbon Nanostructure Electrode with Superior Electrochemical Performance. *Electrochim. Acta* **2020**, *341*, 136045.

(9) Zhou, Y.; Tian, R.; Duan, H.; Wang, K.; Guo, Y.; Li, H.; Liu, H. CoSe/Co Nanoparticles Wrapped by in Situ Grown N-Doped Graphitic Carbon Nanosheets as Anode Material for Advanced Lithium Ion Batteries. *J. Power Sources* **2018**, *399*, 223–230.

(10) Bi, H.; Li, X.; Chen, J.; Zhang, L.; Bie, L. Ultrahigh Nitrogen-Doped Carbon/Superfine-Sn Particles for Lithium Ion Battery Anode. *J. Mater. Sci. Mater. Electron.* **2020**, *31* (24), 22224–22238.

(11) Destyorini, F.; Amalia, W. C.; Irmawati, Y.; Hardiansyah, A.; Priyono, S.; Aulia, F.; Oktaviano, H. S.; Hsu, Y.-I.; Yudianti, R.; Uyama, H. High Graphitic Carbon Derived from Coconut Coir Waste by Promoting Potassium Hydroxide in the Catalytic Graphitization Process for Lithium-Ion Battery Anodes. *Energy & Fuels* **2022**, *36* (10), 5444–5455.

(12) Li, B.; Zhang, Y.; Xiong, J.; Gui, Y.; Huang, T.; Peng, J.; Liu, H.; Yang, F.; Li, M. Chitosan-Derived Graphitic Carbon@Fe3C as Anode Materials for Lithium Ion Battery. *J. Mater. Sci.* **2022**, *57* (22), 9939–9954.

(13) Zhang, C.; Zhang, Z.; Yin, F.; Zhang, Y.; Mentbayeva, A.; Babaa, M.-R.; Molkenova, A.; Bakenov, Z. 3D Ordered Macroporous Carbon Encapsulated ZnO Nanoparticles as a High-Performance Anode for Lithium-Ion Batteries. *ChemElectroChem* **2017**, *4* (9), 2359–2365.

(14) Yin, F.; Zhang, Z.; Zhang, Y.; Zhang, C.; Xu, L. ZnO Nanoparticles Encapsulated in Three Dimensional Ordered Macro-/Mesoporous Carbon as High-Performance Anode for Lithium-Ion Battery. *Electrochim. Acta* **2018**, *270*, 274–283.

(15) Song, L.; Li, L.; Gao, X.; Zhao, J.; Lu, T.; Liu, Z. A Facile Synthesis of a Uniform Constitution of Three-Dimensionally Ordered Macroporous TiO 2 –Carbon Nanocomposites with Hierarchical Pores for Lithium Ion Batteries. *J. Mater. Chem. A* **2015**, *3* (13), 6862–6872.

(16) Shen, K.; Cai, S.; Ling, R.; Xie, D.; Li, X.; Sun, J.; Wei, J.; Sun, X. Flexible, Three-Dimensional Ordered Macroporous ZnO Electrode with Enhanced Electrochemical Performance in Lithium-Ion Batteries. *Microporous Mesoporous Mater.* **2019**, *289*, 109618.

(17) Zhu, X.; Ren, W.; Cheng, C.; Yang, Y. Three-Dimensional Carbon@Fe 2 O 3 @SnO 2 Hierarchical Inverse Opals Arrays as Li-Ion Battery Anode with Improved Cycling Life and Rate Capability. *ChemistrySelect* **2017**, *2* (11), 3223–3230.

(18) Huang, X.; Chen, J.; Lu, Z.; Yu, H.; Yan, Q.; Hng, H. H. Carbon Inverse Opal Entrapped with Electrode Active Nanoparticles as High-Performance Anode for Lithium-Ion Batteries. *Sci. Rep.* **2013**, *3* (1), 2317.

(19) Li, Z.; Tan, Y.; Huang, X.; Zhang, W.; Gao, Y.; Tang, B. Three-Dimensionally Ordered Macroporous SnO2 as Anode Materials for Lithium Ion Batteries. *Ceram. Int.* **2016**, *42* (16), 18887–18893.

(20) McNulty, D.; Carroll, E.; O'Dwyer, C. Rutile TiO 2 Inverse Opal Anodes for Li-Ion Batteries with Long Cycle Life, High-Rate Capability, and High Structural Stability. *Adv. Energy Mater.* **2017**, *7* (12), 1602291.

(21) Shi, Q.; Liu, W.; Qu, Q.; Gao, T.; Wang, Y.; Liu, G.; Battaglia, V. S.; Zheng, H. Robust Solid/Electrolyte Interphase on Graphite Anode to Suppress Lithium Inventory Loss in Lithium-Ion Batteries. *Carbon* **2017**, *111*, 291–298.

(22) Weppner, W.; Huggins, R. A. Determination of the Kinetic Parameters of Mixed-Conducting Electrodes and Application to the System Li3Sb. *J. Electrochem. Soc.* **1977**, *124* (10), 1569–1578.